

# Concentric Fractal Antenna Arrays For Multiband In-Band Full-Duplex

Geili Elsanousi<sup>1</sup>, Franz HIRTENFELDER<sup>2</sup>, Mohammed Abbas<sup>3</sup>, Raed Abd-Alhameed<sup>4</sup>, Xin-She Yang<sup>1</sup>, Tuan Anh Le<sup>1</sup>, and Huan Nguyen<sup>1</sup>

<sup>1</sup>Middlesex University

<sup>2</sup>Dassault Systemes Deutschland GmbH

<sup>3</sup>University of Khartoum

<sup>4</sup>University of Bradford Faculty of Engineering and Informatics

June 30, 2023

## Abstract

Enabling multiband systems with per-band in-band full duplexing (IBFD) opens avenues for multiband instantaneous feedback sensing and streaming. This letter adopts fractal antenna arrays to achieve multiband-IBFD (MIBFD) antenna subsystems using hexagonal star array (HSA) geometry as a generating subarray. Characterised by concentric recurring frequency-independent multiband self-interference cancellation (MB-SIC), the HSA enables a frontier MIBFD stage at the antenna domain. Simulation results confirm this hypothesis using three separately fed 4.9, 5.0 and 5.1 GHz signals as test pilots, which achieved -35.5, -42 and -37 dB SIC respectively and simultaneously. The integrated SIC bandwidth within the band is extended to 4.45 <-> 5.85 GHz below -35.5 dB.

# Concentric Fractal Antenna Arrays For Multiband In-Band Full-Duplex

Geili. T. A. ElSanousi, Franz Hirtenfelder, Mohammed. A.H. Abbas, Raed. A. Abd-Alhameed, Xin-She Yang, Tuan Anh Le, and Huan X. Nguyen

Enabling multiband systems with per-band in-band full duplexing (IBFD) opens avenues for multiband instantaneous feedback sensing and streaming. This letter adopts fractal antenna arrays to achieve multiband-IBFD (MIBFD) antenna subsystems using hexagonal star array (HSA) geometry as a generating subarray. Characterised by concentric recurring frequency-independent multiband self-interference cancellation (MB-SIC), the HSA enables a frontier MIBFD stage at the antenna domain. Simulation results confirm this hypothesis using three separately fed 4.9, 5.0 and 5.1 GHz signals as test pilots, which achieved -35.5, -42 and -37 dB SIC respectively and simultaneously. The integrated SIC bandwidth within the band is extended to 4.45 < - > 5.85 GHz below -35.5 dB.

## Introduction

Full duplex instantaneity, i.e., the ability to route feedback via the receive stream during the transmission instance in the same band and space, is a speciality of the in-band full-duplex (IBFD) techniques. It enables the IBFD receiver to instantly sense and track changes in propagation channels, e.g., channel state information (CSI). IBFD systems control the transmitting inter-element coupling paths to eliminate self-interference (SI) from the receive stream [1, 2].

Concentric circular antenna arrays (CCAA) antenna subsystems generate 360°-steerable beam patterns, enable multi-input multi-output (MIMO) multiplexing or diversity gains under non-uniform excitation [3], and readily scale into massive MIMO arrays [4]. Their symmetry balances coupled paths at the centre, enabling a concentric SI cancellation (SIC). The circular mode phasing (CMP) SIC technique exploits this symmetry by distributing transmit elements in rotational-phased Euclidean angles and using a butler-matrix-like feed circuit to match electrical amplitudes/phases arriving at the centre [2]. Another reference, [5], adopts the orbital angular momentum (OAM) feed of two aligned circular arrays to isolate TX from RX streams. The method implements a non-sequential textitphase-rotation feeding. With an excellent below -40 dB isolation between 13.5 to 16.7 GHz, OAM-IBFD is suitable for directional short-range line-of-sight (LOS) IBFD-MIMO systems given the OAM polarisation stability issues in NLOS environments [5, 6]. The phase-shift precision requirement constrains both methods. This constraint escalates as the number of modes/elements per ring and the corresponding orthogonal Euclidean phases per 360° increase.

In contrast with CMP and OAM methods, a hexagonal star array (HSA) is a two-ring CCAA that adopts the antenna cancellation technique (ACT) [7] to generate a concentric SIC. The ACT *mechanically* maps electrical phases/amplitudes to distances and matches them at the centre. An HSA has a single concentric receive element and twelve transmit elements arranged in hexagonal concentrically-cancelling ACT rings [8]. Its geometry is self-scaling by wavelength multiples with recurring concentric SIC, i.e., a *fractal antenna array* (FAA) [9]. FAAs synthesise scalable multiband arrays of similar electromagnetic characterisation, here the SIC [10]. The letter adopts a fractal HSA (FHSA) structure to achieve broad/multi band SIC at the antenna stage by combining multi-carrier fractals' narrow bands' SIC. Fractal arrays are frequency and polarity independent, i.e., are suitable for both LOS/NLOS links. The fractal methods proposed here serve instantaneous channel sensing applications more than doubling the spectrum.

Single-band SIC is a challenging goal as each IBFD method makes a compromise that limits the SIC. Multiple streams face higher SIC requirements. The SIC figure of merit and bandwidth are inversely related, i.e., more bandwidth implies complex SIC system requirements [11]. To the best of the authors' knowledge, no research in the IBFD field considered enabling independent multiband IBFD (MIBFD) streaming. MIBFD opens an avenue to many applications. e.g., multiband (MB)-CSI for multiband WiFi [12]/massive MIMO systems [13]. The novel adoption of FAAs introduces systematic frequency-independent bandwidth scaling methods to IBFD techniques. The mechanical method outperforms rotational electrical phasing methods, e.g., CMP [2], in scalability as precise feeding phase shifts' requirement does not constrain

it. Also, choosing the HSA geometry inherits its beam steering and multiple MIMO coding feeding features in [8]. Finally, adopting ACT, the cantor map extends the methods in [14] by outlining the optimum feasible ACT pairs co-placements in a 2D aperture.

In this letter we use high-precision CST modelling to validate our concept. The simulations illustrate -35.5, -42, and -37 dB SIC when simultaneously transmitting 4.9, 5.0, and 5.1 GHz signals, respectively, i.e., exceeds the CMP SIC [2]. Results demonstrate integrated concentric multiband (MB)-SIC below -35.5 dB Between 4.45-5.85, a 360° steerable beam, and 7.95-11.97 dBi azimuth/zenith far-field directivity.

## Hexagonal star array fractals

The HSA fractals guide the placement of ACT pairs using wave physics [8]. The practical aperture size bounds the FHSA scalability, the surroundings' antenna reflections and the wave physics changes outside the array's Fraunhofer distance. This section discusses the FHSA fractals' growth modes. FHSA structures expand concentrically, either radially or by rotation, while sharing a concentric MB-SIC. Radial expansions scale HSA rings radially, while rotational ones add ring elements by rotating fractals. Both techniques require a minimum 0.4λ inter-element spacing for mitigated coupling [15].

## Radial Fractal Expansions

For an  $N$ -element antenna array, a null point exits if [8]:

$$\sum_{i=1}^N a_i^2 = -2 \sum_{i=1}^{N-1} \sum_{k=i+1}^N a_i a_k \cos(\Psi_i - \Psi_k), \quad (1)$$

where  $i$  or  $k \in \{1, 2, \dots, N\}$ ,  $a_i$  is the the  $i^{th}$  antenna's carrier amplitude. Assigning the antenna element at  $i=1$  as reference,  $\Psi_i$  defines the phase of the  $i^{th}$  antenna referenced to  $\Psi_1$ . Let  $d_i$  be the distance in wavelengths of the  $i^{th}$  element to the target null, the relationship between  $\Psi_i$  and  $d_i$  is given by  $\Psi_i = 2\pi(d_i - d_1)/\lambda$ . Assuming  $a_i$  is constant over distance, differentiating equation (1) with respect to  $(d_i - d_k)$  leads to:

$$\sum_{i=1}^{N-1} \sum_{k=i+1}^N \frac{2\pi a_i a_k}{\lambda} \sin \frac{2\pi}{\lambda} (d_i - d_k) = 0. \quad (2)$$

A solution set for these derivatives is defined when all  $(d_i - d_k)$  satisfy a phase difference of  $v$  ( $0.5\lambda$ ), i.e.,  $v\pi$  electrical degrees, where  $v$  is a positive integer signifying the radial expansion factor. The second derivative of Eq. (1) identifies the maximum/minimum points at negated cosine functions between (+1) and (-1) for even and odd  $v$  values, respectively. Odd  $v$  values generate null phase sums. Resulting rings follow odd or even tuple-sequence radii patterns. Odd sequence  $\{2n-1.5, 2n-1, 2n-0.5\}\lambda$  seeded by  $(n=2n-1)$  maps symmetric HSA fractals. Even sequence  $\{2n-0.5, 2n, 2n+0.5\}\lambda$  seeded by  $(n=2n)$  maps asymmetric ACT-paired rings. Even/odd or odd/odd rings cancel, but even/even do not.  $n \in \{1, 2, \dots, M\}$  signifies a growth order or a band index for co-located HSA(s).

## Rotational Fractal Expansions

Angular rotation increases the spacing between successive radially expanded HSA fractals or enables placing multiple fractals in the same rings. The centre SIC does not change due to the circular symmetry, but the radiation pattern rotates.

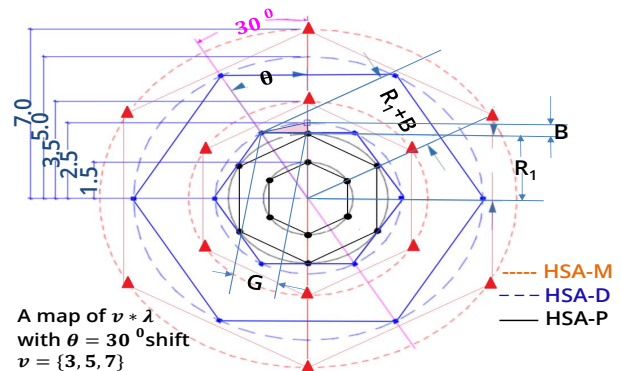


Fig. 1: Inter-element spacing of three HSA fractals.

A) *Increasing the inter-fractal spacing by angular shifts:* Consider three successively co-located scaled-from-single-frequency HSA fractals comprising the 36-elements FHSA shown in Fig. 1, i.e.,  $\{HSA_P, HSA_D, HSA_M\}$ . Inscribed on rings  $\{(0.5 \text{ and } 1.0), (1.5 \text{ and } 2.0), (2.5 \text{ and } 3.0)\}$

3.0), and (2.5 and 5.0) $\lambda$ , the minimum inter-element spacing between these rings is  $0.5\lambda$ .

For a  $\theta^\circ$  angular shift between two successive HSA fractals, if  $R_1$  is the *Inner Radius* and  $R_1+B$  is the *Next Outer Radius* and  $B$  is *before-shift spacing*, by geometry the new spacing  $G$  is derived as  $G = \sqrt{R_1^2 + (R_1 + B)^2 - 2R_1(R_1 + B)\cos(\theta^\circ)} > B$ , hence, angular shifting increases regular FHSA inter-element spacing.

*B) Incorporating more fractals by angular shifts:* As HSA fractals scale radially, the rings' perimeters expand, enabling the alignment of multiple fractals in the same rings obeying the minimum spacing condition. When co-placing multiple frequency angular-rotated HSA fractals in the same rings [8], the chords connecting the inner-ring vertices of successively rotated fractals dictate the minimum inter-element spacing. Assigning  $Q$  as the number of valid rotated HSA fractals within a ring, the value of  $Q$  equals the inner HSA chord length  $C_{in}$  divided by the minimum spacing  $0.4\lambda$ , approximated to  $0.5\lambda$ . The hexagon side equals its radius, i.e.,  $C_{in} = 0.5v\lambda$ , for an odd sequence scaled by a factor  $v$ , hence:

$$Q = \frac{0.5v\lambda}{0.5\lambda} = v. \quad (3)$$

If  $Q$  shifts are implemented, given the hexagonal angle is  $60^\circ$ , the possible rotation angle  $\theta$  for a ring will be  $\theta = 60/Q$  and the angular shift index is  $q \in \{1, 2, \dots, Q\}$ . The chord length  $P$  between inner-ring vertices of two successively rotated fractals is greater than or equal to  $0.5\lambda$ , i.e.:

$$P = 2C_{in} \sin \frac{\theta}{2} = \lambda \left( v \sin \frac{30}{v} \right) \geq 0.5\lambda. \quad (4)$$

*C) HSA Cantor Maps:* Combining radial and rotational expansions leads to a cantor map entailing the FHSA expansions. i.e., the optimum ACT pairs' co-placements in a CCAA. A single-frequency HSA fractal generates the wavelength-based map shown in Fig. 2. This map maintains a minimum spacing greater than  $0.4\lambda$  between all elements/rings. Developing FHSA structures requires selecting different sets of  $\{v, n, q\}$  from  $M$ -carriers' maps, e.g.,  $\{5, 3, 1\}$  as illustrated. FHSA structures inherit HSA's multiple ACT pairs streaming options in [8].

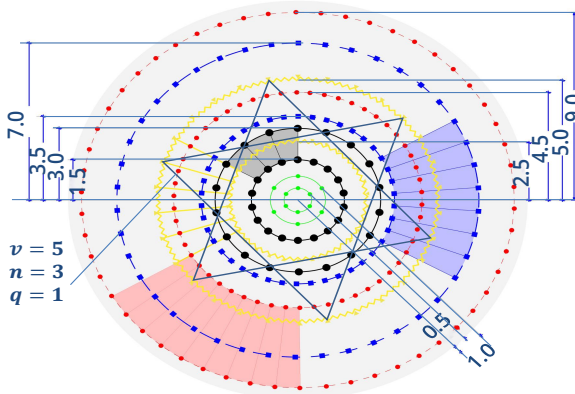


Fig. 2: Single Frequency HSA Cantor map for odd  $v$  multiples.

*D) HSA-Fractal Array Design and Simulation Model:* Figure. 3 demonstrates a unit cell comprising a wire-monopole from-coaxial with a ground circular copper disk, an FR-4 disk of dielectric constant 4.3 on top of the ground, and the element modelled using the H500 standard dimensions. The defected ground circular disk wire monopole gives value to further reduce the mutual coupling and enables flexible real times control on placing array elements.

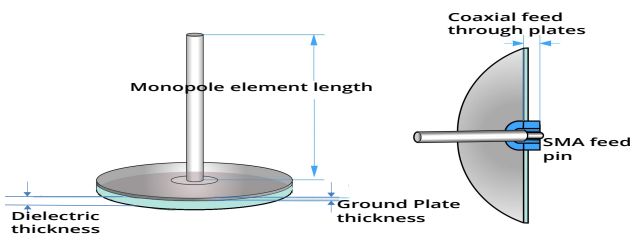


Fig. 3: Antenna monopole unit cell.

The experimental setup deploys a 36 unit cells transmitting array (TX) comprised of 3 HSA-fractals, i.e.,  $HSA_P$ ,  $HSA_D$ , and  $HSA_M$ ,

following Fig. 1. The 37<sup>th</sup> receiving element (RX) is in the centre. In the initial simulations, the FHSA fractals are fed via 36, one-watt power, zero degrees phase, wave-guide ports and transmit 5.1, 5.0 and 4.9 GHz respective bands simultaneously for  $n \in \{1, 2, 3\}$  expansion levels and a scaling factor set  $v \in \{3, 5, 9\}$ . Rings  $v \in \{1, 7\}$  were thinned to mitigate mutual coupling impacts. The HSA-D fractal at  $\{v, n, q\} = \{5, 2, 2.5\}$  is rotated by  $30^\circ$  angle.

#### Simulation setup and results

The model is simulated in 3 phases; phase 1 optimises TX array elements' geometry, phase 2 optimises TX weights for a centre E-field null, and phase 3 measures the RX MB-SIC.

*A) Optimising Geometry of TX Array Elements:* The electromagnetic model characterisation is simulated using CST microwave studio. The geometry is optimised using the monopole length, ground radius, and dielectric plate thickness as parameters to obtain the best TX  $s$ -parameters in Fig. 4. The figure demonstrates the inner and outer  $HSA_P$  ( $S1$  and  $S2$ ),  $HSA_D$  ( $S101$  and  $S102$ ), and  $HSA_M$  ( $S1001$  and  $S1002$ ) rings'  $s$ -parameters respectively. By CCAA ring symmetry, one ACT pair reflects the rest HSA pairs' responses. The overlapped return bandwidth is 4.88 to 5.31 GHz.

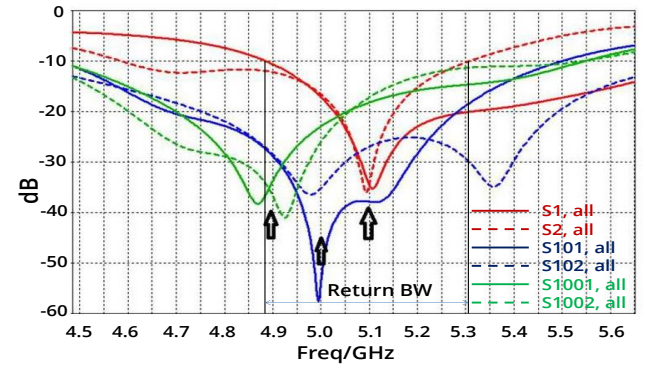


Fig. 4: Simultaneously optimised S-parameters.

These parameters are then matched using a correction factor  $S_{ii}/\sqrt{1-S_{ii}^2}$ , where  $S_{ii}$  is element  $i$ 's  $s$ -parameter. This step reduces the design amplitude mismatches in an initial simulation run [16]. The centre E-field readings after matching the S-parameters improved from 25000V/m to 150V/m.

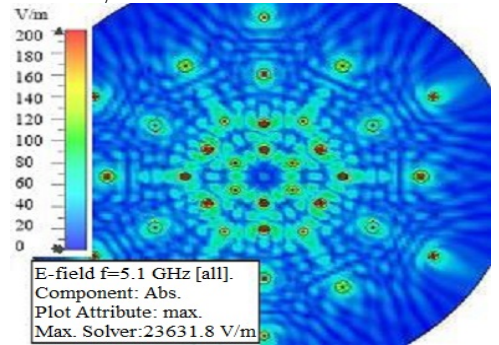


Fig. 5: Initial noisy null point.

*B) Optimising TX Feed Weights for Balanced Centre Null:* With transmit array elements' geometry optimised, feed phases and amplitudes are optimised for an optimum centre SIC goal. A technical problem hinders simultaneous optimisation. The CST environment is based on single reference-frequency Fourier transforms, while the test signal comprises three frequencies. The finite integration technique is used in a time-domain formulation to answer this challenge.

The leap-frog time-integration algorithm is applied to Maxwell's equations' integral form. Time signals received at ports are recorded and converted into frequency domain data to compute the simultaneous S-parameters for all elements. Unknowns of the system-matrix, i.e., edges at the six sides of the Hexa-mesh<sup>1</sup> elements are simultaneously transferred via a corresponding discrete Fourier transform for each fractal and superimposed to obtain the simultaneous frequency response.

<sup>1</sup> CST Geometries are approximated as a sequence of concatenated hexagonal 3D structures, or Hexa-meshes, for which E/H fields are computed [17].

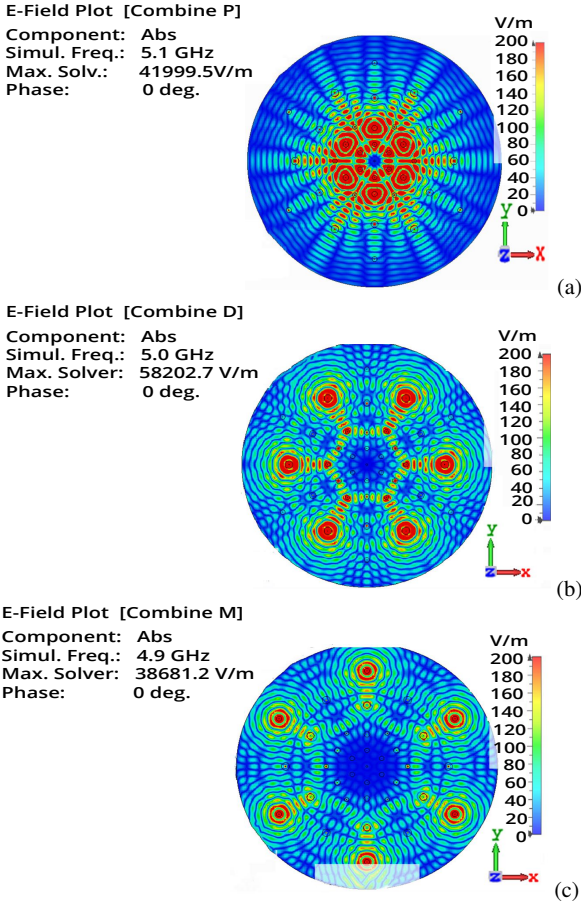


Fig. 6: 2D scans of optimised near E-field null at centre for (a):  $HSA_P$  fractal; (b):  $HSA_D$  fractal; (c):  $HSA_M$  fractal.

Following the above setup, the solver is run in sequential mode to generate a  $12 \times 12$  S-parameters matrix for each HSA subarray at the respective frequency. For each array result, a post-processing optimisation goal function is set for a zero  $V/m$  at the centre by varying amplitudes and phases using the trusted region framework algorithm [18]. Figure. 6 illustrates 0  $V/m$  null in all fractals' optimised near-fields. The cavity radius is proportional to the array aperture, and  $HSA_D$  angular rotation does not affect SIC.

**C) Integrated Near-Field Results:** The resulting fields of the three optimised arrays are combined using a post-processing template. The optimised feeds compensate outer/inner rings' phase/amplitude mismatches, as in real-time effects. Table. 1 demonstrates 4.15, 12.16°, and 8.32° phase mismatches. The combined e-fields demonstrate a perfect concentric null as shown in Fig. 7.

Array.	O. Amplitude.	O. Phase.	I. Amplitude.	I. Phase.
$HSA_P$	1.425W	-21.76°	0.476W	-25.91°
$HSA_D$	2.00W	-24.31°	1.00W	-12.15°
$HSA_M$	1.69W	-60.36°	1.14W	-52.68°

**Table 1:** Optimised amplitude/phase feeds

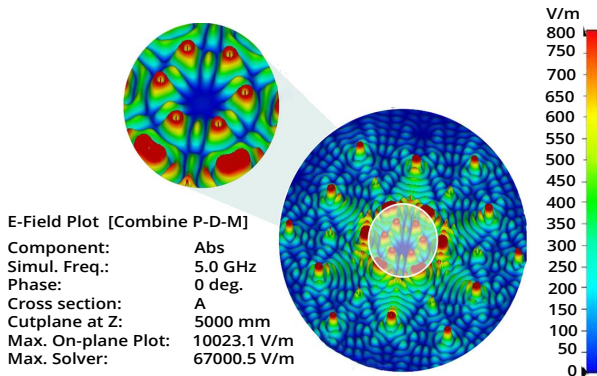


Fig. 7: 3D combined SIC with null centre E-field.

**D) Measuring the Multi-Band SIC via RX:** The RX centre port is next included in the simulation. Figures 8(a) and (b) depict the SIC curves, i.e., the power absorbed by the centre receiving port divided by the total TX array power. The fractals  $HSA_P$ ,  $HSA_D$ , and  $HSA_M$  generate, respectively, three SIC figures -35.5 dB, -42 dB, and -37 dB, as shown in Fig. 8 (b). The SIC bandwidth below -30 dB spans from 4.45 to 5.85 GHz frequency, i.e., introducing the multiband fractals increases the IBFD operating bandwidth. Fig. 8 (b) will be used to make a comparison with a baseline later in Section .

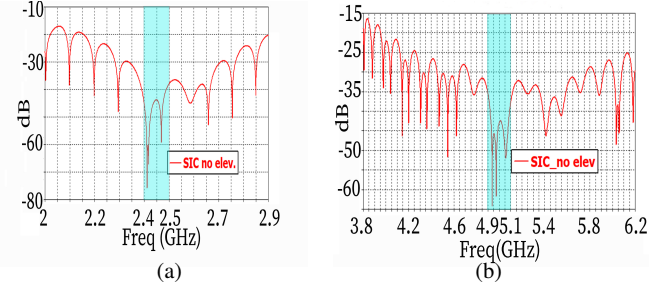


Fig. 8: Multiband SIC curves without elevating the centre (a) 4.9-5.1 GHz and (b) 2.4-2.5 GHz bands.

**E) Far-Field Results:** Far-field results reflect the array performance with the optimised centre SIC. Defected ground monopole generates a dipolic pattern with an array pattern symmetric about  $\theta = 0^\circ$ . The combined far-field results from  $\theta$  equals  $-180^\circ$  to  $0^\circ$  are demonstrated in Fig. 9. The closely similar  $\theta$  equals  $0^\circ$  to  $180^\circ$  pattern is omitted for image clarity.

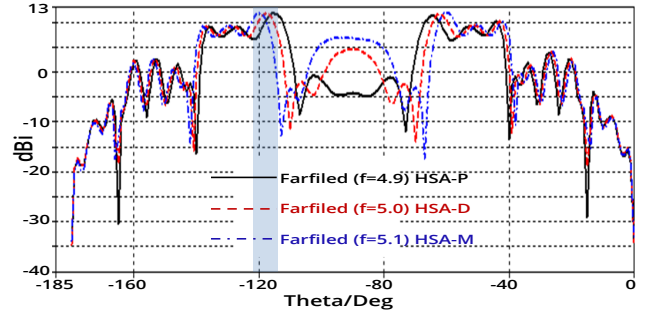


Fig. 9: Farfield directivity (Abs,  $\phi = 0$ ) from  $\theta = -180^\circ$  to  $0^\circ$ .

The far-field patterns vary closely in these narrow bands. Deploying more fractals at more bands may result in wider space/frequency-division combinations as shaded between  $\theta = -122^\circ$  to  $-112^\circ$ . Varying the feeding weights of antenna cancelling pairs steers the beams. Rotating  $HSA_D$  by  $30^\circ$  steers the constant  $\phi$  radiation pattern.

**F) Baseline Comparisons :** We compare our approach with a baseline implementing CMP, in which the centre RX is elevated using a metal cylinder along the z-axis to increase the isolation as adopted in [2] Fig. 4(b). For comparison, 2.4, 2.45, and 2.5 GHz and 4.9, 5.0 and 5.1 GHz elevated FHSA models are developed. Because FHSA models use defected ground, a dielectric insulating plate isolates the cylinder from the elevated RX.

Cylinders were optimised for best SIC varying height/radius. Optimum heights/radii measured 295/31 mm and 539/43 mm for the above FHSA models, respectively. The CMP technique cylinder's height/radius measured 76/51 mm at 2.4-2.5 GHz band [2]. The difference in aperture sizes between the two techniques justify this disparity. Figures. 10 (a) and (b) demonstrate elevated SIC curves.

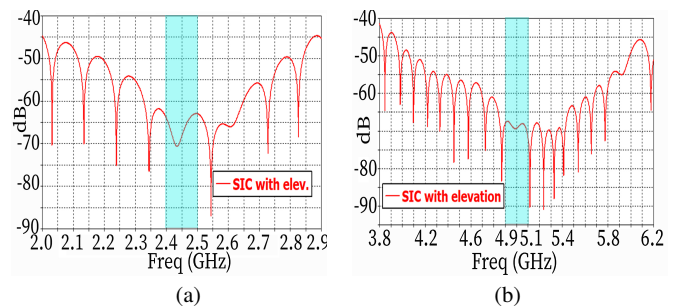


Fig. 10: SIC figure for two centre-elevated FHSA fractals (a) 2.4-2.5 GHz and (b) 4.-5.1 GHz. Desired bands are shaded.

The hardware results in [2] consolidate previous HSA-SIC simulations in [8]. In Fig. 8 (b) [2], the blue curve measures -30 dB elevated RX SIC when the cylinder shadows a single element. The red curve measures -60 to -65 dB SIC by combining CMP with RX elevation, i.e., the CMP contributes -30 to -35 dB SIC, similar to the -30 dB SIC using 2.4 GHz HSA in [8]. This SIC is improved to below -45 dB between 2.4 – 2.5 GHz using non elevated FHSA in Fig. 8 (a).

Contrasting Figs. 8 (a)/(b) with Figs. 10 (a)/(b) and CMP, the elevation enhances the SIC by comparative figures, a -25 to -35 dB rough average contribution., i.e., elevation impact is independent of the frequency or the technique. The 2.4 – 2.5 GHz FHSA delivers flatter SIC variations over bandwidth compared to the 4.9-5.1 GHz FHSA due to higher mutual coupling impact at higher frequencies, i.e., mutual coupling reduction techniques [16] are required for higher frequency FHSA. The elevated FHSA illustrated higher SIC compared to the elevated CMP at both designated bands with an average extra 5 – 12 dB SIC.

### Conclusion

This letter introduces a method to attain frequency-independent MIBFD streaming. The HSA geometry is adopted as a fractal subarray with recurring concentric MB-SIC. The letter analyses the fractal recursion under constraints of a  $0.4\lambda$  minimum distance between elements and tests conditions for maximising the aperture efficiency by radial/angular fractals' expansions. The results demonstrate integrated MB-SIC curves.

G. T. A. Elsanousi, X. -S. Yang, T. A. Le, and H. X. Nguyen are with the Department of Design Engineering & Mathematics, Middlesex University, The Burroughs, Hendon, London, U.K.

Email: {g.t.elsanousi; x.yang; t.le; h.nguyen}@mdx.ac.uk.

F. Hirtenfelder is with Dassault Systèmes, STEP Stuttgarter Engineering Park GmbH, Germany.

Email: franz.hirtenfelder@3ds.com

M. A. H Abbas is with Faculty of Engineering, University of Khartoum, P. O. Box 321, 11111, Khartoum.

Email: mabbas@uofk.edu.sd

R. A. A. Alhameed is with RF laboratory, university of Bradford, Richmond Rd, Bradford BD7 1DP.

Email: r.a.a.abd@brad.ac.uk.

### References

- 1 T. Zhang, S. Biswas, and T. Ratnarajah, "An analysis on wireless edge caching in in-band full-duplex fr2-iab networks," *IEEE Access*, vol. 8, pp. 164 987–165 002, 2020.
- 2 K. E. Kolodziej, P. T. Hurst, and A. J. Fenn, "Evolution of circular mode phasing for in-band full-duplex omnidirectional antennas," *IEEE Trans. Antennas Propag.*, vol. 69, no. 11, pp. 7145–7155, 2021.
- 3 G. Sun, Y. Liu, Z. Chen, S. Liang, A. Wang, and Y. Zhang, "Radiation beam pattern synthesis of concentric circular antenna arrays using hybrid approach based on Cuckoo search," *IEEE Trans. Antennas Propag.*, vol. 66, no. 9, pp. 4563–4576, 2018.
- 4 E. Anarakifirooz and S. Loyka, "Favorable propagation for massive MIMO with circular and cylindrical antenna arrays," *IEEE Wireless Commu. Lett.*, 2021.
- 5 Y.-M. Zhang and J.-L. Li, "An orbital angular momentum-based array for in-band full-duplex communications," *IEEE Ant. and Wirel. Propag. Lett.*, vol. 18, no. 3, pp. 417–421, 2019.
- 6 Y. Yang and W. Luo, "Analysis of orbital angular momentum electromagnetic wave propagation based on circular antenna array," in *2017 Prog. in Electromag Research Symp - Fall (PIERS - FALL)*, 2017, pp. 605–609.
- 7 J. I. Choi, M. Jain, K. Srinivasan, P. Levis, and S. Katti, "Achieving single channel, full duplex wireless communication," in *Proc. of the 16th annu. int. conf. on Mobi. compu. and netw.*, 2010, pp. 1–12.
- 8 G. T. A. El Sanousi, F. Hirtenfelder, M. A. Abbas, R. A. Abd-Alhameed, X.-S. Yang, T. A. Le, and H. X. Nguyen, "The peculiar case of the concentric circular hexagonal-star array: Design and features," in *28th Int. Conf. Telecom. (ICT)*, 2021, pp. 1–6.
- 9 P. Felber, "Fractal antennas," *Illinois Institute of Technology*, 2000.
- 10 D. Werner, M. Gingrich, and P. Werner, "A self-similar fractal radiation pattern synthesis technique for reconfigurable multiband arrays," *IEEE Trans. on Antennas and Propag.*, vol. 51, no. 7, pp. 1486–1498, 2003.
- 11 K. E. Kolodziej, *In-Band Full-Duplex Wireless Systems Handbook, ch1., pp. 20-35, ch2., pp. 36-41, ch 5., pp.33-48*, 1st ed. Artech House, 2021.

- 12 D. Wang and C. H. Chan, "Multiband antenna for wifi and wigo communications," *IEEE Antennas and Wireless Propag. Letters*, vol. 15, pp. 309–312, 2016.
- 13 Q.-U.-A. Nadeem, A. Kammoun, M. Debbah, and M.-S. Alouini, "Design of 5G full dimension massive MIMO systems," *IEEE Trans. Commun.*, vol. 66, no. 2, pp. 726–740, 2018.
- 14 M. A. Khojastepour, K. Sundaresan, S. Rangarajan, X. Zhang, and S. Barghi, "The case for antenna cancellation for scalable full-duplex wireless communications," in *Proc. of the 10th ACM Wkshp on Hot Topics in Networks*, 2011, pp. 1–6.
- 15 H. Li, G. Zhaozhi, M. Junfei, J. Ze, L. ShuRong, and Z. Zheng, "Analysis of mutual coupling effects on channel capacity of MIMO systems," in *IEEE Int. Conf. on Netw., Sens. and Ctrl.* IEEE, 2008, pp. 592–595.
- 16 J.-Y. Guo, F. Liu, G.-d. Jing, L.-y. Zhao, Y.-z. Yin, and G.-l. Huang, "Mutual coupling reduction of multiple antenna systems," *Frontiers Info. Techno. Elect. Eng.*, vol. 21, no. 3, pp. 366–376, 2020.
- 17 M. Malzacher, L. R. Schad, and J. Chacon-Caldera, "Comparison of time and frequency domain solvers for magnetic resonance coils at different field strengths using a single computational platform," *IEEE J. of Electromag, RF and Microw. in Med. and Bio.*, 2021.
- 18 Y.-X. Yuan, "A review of trust region algorithms for optimization," in *Iciam*, vol. 99, no. 1, 2000, pp. 271–282.